Enhanced Photocatalytic Activity of Au/TiO₂ Nanoparticles against Ciprofloxacin

Pedro Martins [1,2,*], **Sandro Kappert** [3], **Hoai Nga Le** [3,4], **Victor Sebastian** [5,6], **Klaus Kühn** [3], **Madalena Alves** [1], **Luciana Pereira** [1], **Gianaurelio Cuniberti** [3,7,8], **Manuel Melle-Franco** [9] **and Senentxu Lanceros-Méndez** [1,10,11,*]

1   Department of Physics/Centre of Biological Engineering, University of Minho, 4710-057 Braga, Portugal; madalena.alves@deb.uminho.pt (M.A.); lucianapereira@deb.uminho.pt (L.P.)
2   IB-S—Institute for Research and Innovation on Bio-Sustainability, University of Minho, 4710-057 Braga, Portugal
3   Institute for Materials Science and Max Bergmann Center of Biomaterials, Technische Universität Dresden Dresden, 01062 Dresden, Germany; sandro_kappert@web.de (S.K.); hnle@nano.tu-dresden.de (H.N.L.); klaus.kuehn@nano.tu-dresden.de (K.K.); gianaurelio.cuniberti@tu-dresden.de (G.C.)
4   Department of Chemical Engineering, Hanoi University of Science and Technology, Hanoi 10000, Vietnam
5   Department of Chemical Engineering, Aragon Institute of Nanoscience (INA), University of Zaragoza, Campus Río Ebro-Edificio I+D, C/Poeta Mariano Esquillor S/N, 50018 Zaragoza, Spain; victorse@unizar.es
6   Networking Research Centre on Bioengineering, Biomaterials and Nanomedicine, Centro de Investigacion Biomédica en Red—Bioengenharía, Biomateriales e Nanomedicina, 28029 Madrid, Spain
7   Dresden Center for Computational Materials Science, Technische Universität Dresden Dresden, 01062 Dresden, Germany
8   Center for Advancing Electronics Dresden, Technische Universität Dresden Dresden, 01062 Dresden, Germany
9   Centro de Investigação em Materiais Cerâmicos e Compósitos, Aveiro Institute of Materials, Department of Chemistry, University of Aveiro, 3810-193 Aveiro, Portugal; manuelmelle.research@gmail.com
10 BCMaterials, Basque Center for Materials, Applications, and Nanostructures, Universidad del País Basco—Euskal Herriko Unibertsitatea, Science Park, 48940 Leioa, Spain
11 IKERBASQUE, Basque Foundation for Science, 48013 Bilbao, Spain
*   Correspondence: pamartins@fisica.uminho.pt (P.M.); senentxu.lanceros@bcmaterials.net (S.L.-M.)

Abstract: In the last decades, photocatalysis has arisen as a solution to degrade emerging pollutants such as antibiotics. However, the reduced photoactivation of TiO₂ under visible radiation constitutes a major drawback because 95% of sunlight radiation is not being used in this process. Thus, it is critical to modify TiO₂ nanoparticles to improve the ability to absorb visible radiation from sunlight. This work reports on the synthesis of TiO₂ nanoparticles decorated with gold (Au) nanoparticles by deposition-precipitation method for enhanced photocatalytic activity. The produced nanocomposites absorb 40% to 55% more radiation in the visible range than pristine TiO₂, the best results being obtained for the synthesis performed at 25 °C and with Au loading of 0.05 to 0.1 wt. %. Experimental tests yielded a higher photocatalytic degradation of 91% and 49% of ciprofloxacin (5 mg/L) under UV and visible radiation, correspondingly. Computational modeling supports the experimental results, showing the ability of Au to bind TiO₂ anatase surfaces, the relevant role of Au transferring electrons, and the high affinity of ciprofloxacin to both Au and TiO₂ surfaces. Hence, the present work represents a reliable approach to produce efficient photocatalytic materials and an overall contribution in the development of high-performance Au/TiO₂ photocatalytic nanostructures through the optimization of the synthesis parameters, photocatalytic conditions, and computational modeling.

Keywords: Au-TiO₂; antibiotics; emergent contaminants; nanocatalyst; photocatalysis; GFN-xTB

1. Introduction

The resilience of specific emerging pollutants such as pharmaceuticals to the traditional wastewater treatments makes them spread in variable concentrations in surface and groundwater [1]. Dissemination of antibiotics in nature is one of the most significant environmental concerns as they affect biological metabolism and induce the presence of bacterial resistance among drinking water sources [2]. Photocatalysis has received considerable attention from the scientific community as a possible solution to degrade these compounds [3,4].

Typically, the photocatalytic process takes place when a catalyst is UV irradiated and electron-hole pairs are created that will react with H_2O, OH^-, and O_2 to generate oxidizing species such as the hydroxyl radical ($OH\bullet$), superoxide radical anions ($O_2\bullet-$), and hydrogen peroxide (H_2O_2). These species will initiate a series of reactions that will degrade pollutants into harmless compounds (e.g., CO_2 and H_2O).

Photocatalysis presents several advantages when compared with other methods, such as the low cost, and the eco-friendly and straightforward processing conditions [5,6]. Many photocatalysts have been reported in the last decades [7,8]. Among them, titanium dioxide (TiO_2) is the most studied and applied in photocatalysis, mainly because of its remarkable optical and oxidizing properties, superhydrophilicity, chemical stability, and durability [9,10]. Despite the compelling advantages of TiO_2, there are also some drawbacks. One of the main hurdles is the low spectral activation of TiO_2, caused by its wide bandgap (3.0–3.2 eV) excitation that only occurs under radiation in the UV or near the UV region (410–387 nm) [11].

For this reason, solar radiation cannot be efficiently used because only less than 5% of this radiation corresponds to UV [3]. Additionally, the process becomes less cost effective as the UV lamps are required to provide the radiation. Another limitation is the electron-hole pair recombination that decreases the photocatalytic efficiency [12,13].

The research developed in the last decades has been mainly devoted to surpassing those limitations by producing new and more efficient photocatalytic materials. Strategies for metallic and nonmetallic doping, co-doping [14,15], dye sensitization, semiconductor combination, co-catalyst loading, and nanocomposite materials [16,17] have been used and tested. These approaches allow us to reduce the electron-hole recombination rate and enhance the absorption of visible radiation of TiO_2 by introducing intermediate energy levels inside the bandgap [18]. In this scope, several works have reported the functionalization of TiO_2 nanoparticles surfaces with metals such as Au [19], Cu [20], Co [21], and Ag [22]. When irradiated, noble metals nanoparticles at the TiO_2 surface can receive electrons and prevent the recombination of the photo-generated electron-hole pairs [23,24].

Metals such as Au and Ag can increase visible light absorption due to the surface plasmon resonance effect [25,26]. Gold (Au) nanoparticles have attracted considerable attention, mainly because they possess exceptional stability, nontoxicity, and biocompatibility [3]. Their properties are highly dependent on the size and shape of the nanoparticles, allowing a broad range of applications [27,28]. For instance, the literature shows that gold nanoparticles in the range of 5 to 10 nm present an enhanced catalytic activity [29,30]. In this sense, some works focused on the photocatalytic activity of Au/TiO_2 nanocomposite have been published, including interesting review articles [3,29,31].

Different physical-chemical techniques have been exploited to produce Au/TiO_2 nanocomposites with enhanced catalytic properties. For instance, chemical vapor deposition [32], sol-gel [33], spray pyrolysis [34], electrophoretic approach [35], deposition-precipitation (DP) [36], deposition-precipitation using urea [37], impregnation [38], hybridization [39], and surface functionalization [40], among others [41,42]. However, many of these techniques are time-consuming, and few of them have focused on the optimization of the nanocomposite and the computational modeling of its nanostructure. Thus, this work focused on the optimization of a DP, converting the Au/TiO_2 nanocomposite production into a cost-effective and straightforward technique, with enhanced photocatalytic activity, under UV and visible radiation. The method optimization aims for cost reduction, using the lowest Au loading that endows visible spectra photocatalytic activity to the nanocomposite. The computational studies

provide further information about the electronic mechanism behind the enhanced photocatalytic activity of the Au/TiO$_2$ nanocomposite, as well as the interaction with the target compound.

The target compound is the fluoroquinolone ciprofloxacin (CIP) (chemical formula in Supplementary Material, Figure S1), belonging to a class of synthetic broad-spectrum antibiotics [43], which is mostly used in medicine (e.g., tuberculosis, pneumonia, or digestive disorders). It is also one of the most prescribed fluoroquinolones in the world and studies has shown its presence in potable water and wastewater, as well as in sewage sludge at variable concentrations from milligrams to nanograms per liter [2,44].

In this work, photocatalytic efficiency during the degradation of CIP under UV and visible illumination was assessed. To the best of our knowledge, this is the first work that combines an optimization process of Au/TiO$_2$ nanocomposite with photocatalytic experiments for CIP degradation and computational modeling that addresses the interaction between Au and TiO$_2$ nanoparticles, as well as the interaction of CIP with the produced nanocomposites.

2. Results and Discussion

2.1. Nanocomposite Characterization

The Au/TiO$_2$ nanocomposites were produced by nanoprecipitation method, and the temperature (25, 60, and 80 °C) and the Au loading (ranging from 0.025 to 0.5 wt. %) were changed to understand how these parameters affect the morphology of the nanocomposites and relate it to the photocatalytic efficiency. In this sense, scanning transmission electron microscopy-high-angle annular dark-field imaging (STEM-HAADF) analysis was performed, and the micrographs of the different nanocomposites are displayed in Figure 1.
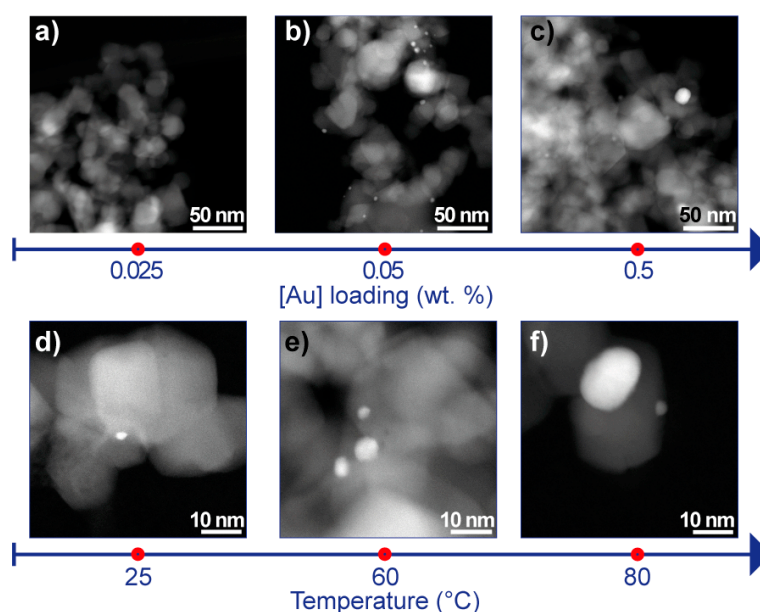

Figure 1. Scanning transmission electron microscopy-high-angle annular dark-field imaging micrographs of Au/TiO$_2$ nanocomposites synthesized with different Au loadings at 60 °C (**a–c**), and Au/TiO$_2$ nanocomposites obtained at different temperatures with an Au loading of 0.05 wt. % (**d–f**).

The Au loading study (Figure 1a–c) was assessed producing different nanocomposites using the same experimental conditions (temperature = 60 °C) and changing the loading of gold exclusively, from 0.025 to 0.5 wt. %. The STEM-HAADF micrographs show that for the sample with 0.025 wt. % of Au (Figure 1a), the presence of Au nanoparticles over the surface of the TiO$_2$ nanoparticles was almost inexistent (Figure 1a). With the increase of Au loading to 0.05 wt. % (Figure 1b), it was possible to observe a homogeneous distribution of predominantly small Au nanoparticles (bright contrast

nanoparticles below 5 nm in diameter) over the TiO$_2$ nanoparticles. Similar results were obtained for 0.1 wt. % (data not shown). For the concentrations of 0.25 and 0.5 wt. % (Figure 1a–c), agglomerates of Au over theTiO$_2$ nanoparticles (brightest areas of the micrograph) were identified as well as large Au nanoparticles. Analogously, the effect of temperature on the synthesis product was also performed maintaining all the synthesis parameters (Au loading = 0.05 wt. % yielded a homogeneous distribution and size of Au nanoparticles) and changing the temperature of the different samples. STEM-HAADF images (Figure 1d–f) indicate that although the used Au loading was the same in the three temperatures tested when the nanocomposite was synthesized at 80 °C, larger Au nanoparticles appeared more frequently on the nanocomposite (Figure 1f). Conversely, at lower temperatures (25 and 60 °C), the Au nanoparticles size was smaller (Figure 1d,e).

The study of the effect of Au loading and temperature in the nanocomposites morphology indicates that the samples produced at 60 °C and with an Au loading of 0.05 wt. % possessed the more homogeneous distribution and size of Au nanoparticles. In this way, a more detailed STEM-HAADF analysis (Figure 2) was performed on this sample. Figure 2a,b reveal a homogeneous dispersion of Au nanoparticles (white arrows) over TiO$_2$ nanoparticles' surface. The representation of the sphere-like shape of Au nanoparticles in Figure 2c, where an high-resolution scanning transmission electron microscopy – high-angle annular dark field shows that single-crystal nanoparticles with high crystallinity were produced by the proposed method. Size distribution, ranging from 1 to 7 nm, and the average size of 3.2 ± 1.13 nm (Figure 2d), were quantified using Image J software applied to 400 nanoparticles. The size distribution of Au nanoparticles for synthesis at 25 °C and 80 °C is provided in Supplementary Material (Figure S2). All the images show Au nanoparticles with similar sizes, which is in good agreement with the size distribution histogram that presents a sharp size distribution.
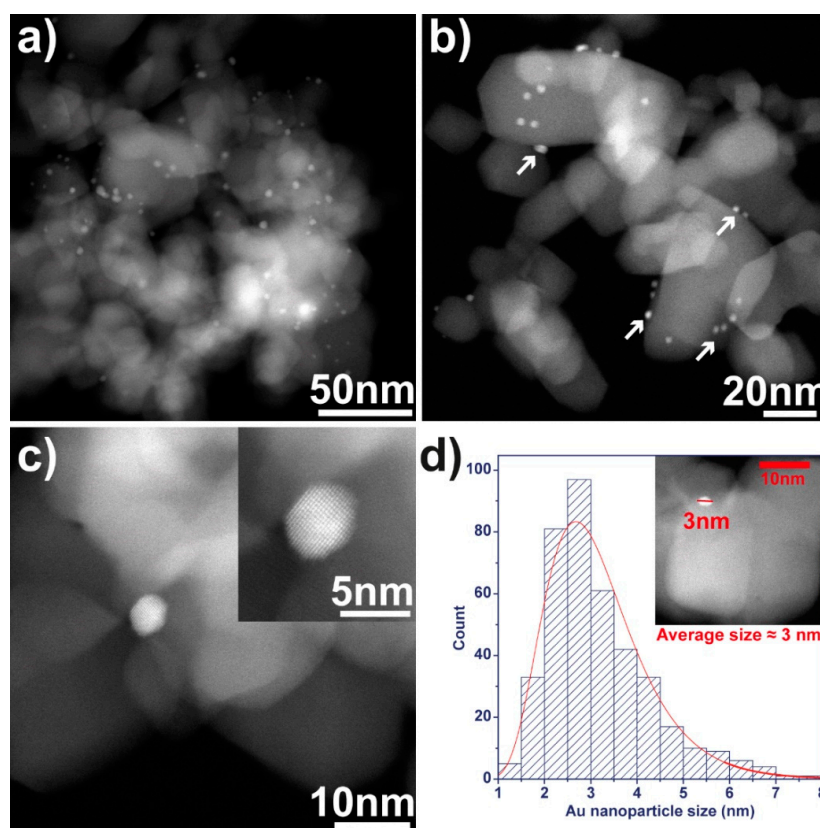
Figure 2. STEM-HAADF micrographs of Au/TiO$_2$ nanocomposites (produced at 60 °C and Au loading of 0.05 wt. %) at different scales (**a**) 50 and (**b**) 200 nm; detail of Au nanoparticle over TiO$_2$ nanoparticles' surface and single Au nanoparticle amplification (inset) (**c**); size distribution of 400 Au nanoparticles with the respective average size (**d**).

The STEM-HAADF- energy-dispersive X-ray spectroscopy (EDX) measurements allowed us to identify the elements present in the Au/TiO$_2$ sample in two different points, 1 and 2 (signaled in Figure 3a). STEM-HAADF-EDX spectra in Figure 3b in point 1 indicate the presence of Au and Cu (copper), which can be respectively addressed to Au nanoparticles and copper grid. In point 2, the signatures of Ti (titanium) and O (oxygen) were identified, corresponding to TiO$_2$ nanoparticles. Thus, EDX measurements confirmed the presence of all the elements of the Au/TiO$_2$ nanocomposite.
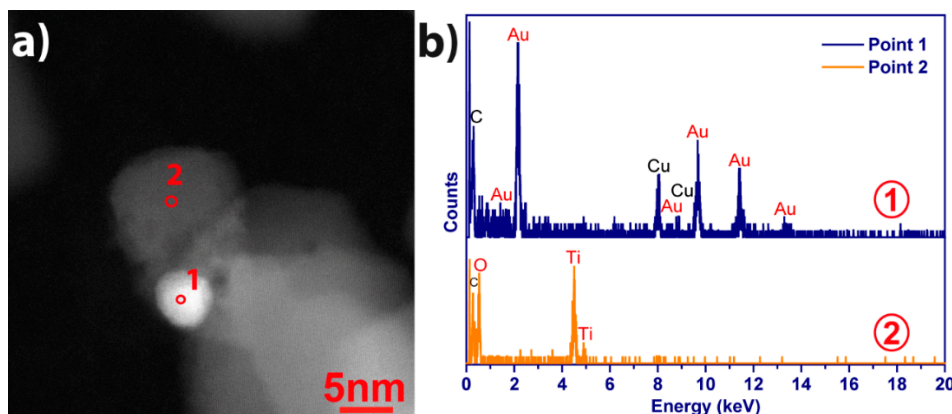
Figure 3. The STEM-HAADF- energy-dispersive X-ray spectroscopy (EDX) image of Au/TiO$_2$ nanocomposites with the identification of the measured points: Au (1) and TiO$_2$ (2) (**a**), EDX spectra with elemental identification (Au, Ti, O, and C) for points 1 and 2 (**b**). The Au/TiO$_2$ nanocomposite synthesized at 60 °C and with an Au loading of 0.05 wt. % was used.

X-ray diffraction was performed to assess the crystal structure of the pure TiO$_2$ nanoparticles and Au/TiO$_2$ nanocomposite, Figure 4a. Both samples show the typical reflexes from anatase (25.3°, 37.8°, and 48.0°) and rutile (27.49°). There was no significant difference between the intensities or positions of the reflexes from both samples. Moreover, no reflexes of Au were detected, which can be explained by the low amount of Au present in the nanocomposite (below detection limit). Figure 4b shows the study of hydrodynamic size for TiO$_2$ and Au/TiO$_2$ nanocomposites obtained by dynamic light scattering (DLS). The results indicated nanoparticles diameters of 1023 nm and 342 nm, for the pristine TiO$_2$ and the Au/TiO$_2$ nanocomposites, respectively. The results suggest that the presence of Au nanoparticles over TiO$_2$ nanoparticles surface may prevent the formation of nanoparticles' aggregates. On the other hand, the size distribution was broader for the nanocomposites regarding the pristine TiO$_2$. Previous work equally showed that the presence of erbium (Er) on TiO$_2$ nanoparticles contributed to reducing the hydrodynamic size when compared with bare TiO$_2$ [15].

The zeta potential was studied at different pH values (3, 5, 7, 9, and 11) for TiO$_2$ and Au/TiO$_2$ samples and the results are displayed in Figure 4c. The pristine and the Au/TiO$_2$ presented very similar profiles, with higher zeta potential values ≈ |20| mV for pH below 3 and 9. These data were in good agreement with the literature [45], with positive zeta potential values for acidic conditions and negative values for basic pH. The more significant difference between the two samples occurred at pH = 7, with the nanocomposite presenting higher zeta potential values than the pure TiO$_2$. Higher zeta potential values mean that nanoparticles possess higher periphery surface charge, which promotes nanoparticles' repulsions, avoiding aggregates' formation and enhanced stability [46]. In this context, and relating it with DLS-obtained results, the smaller hydrodynamic size was probably obtained for the Au/TiO$_2$ because repulsions endowed by Au on TiO$_2$ nanoparticles surface prevented the formation of the aggregates.
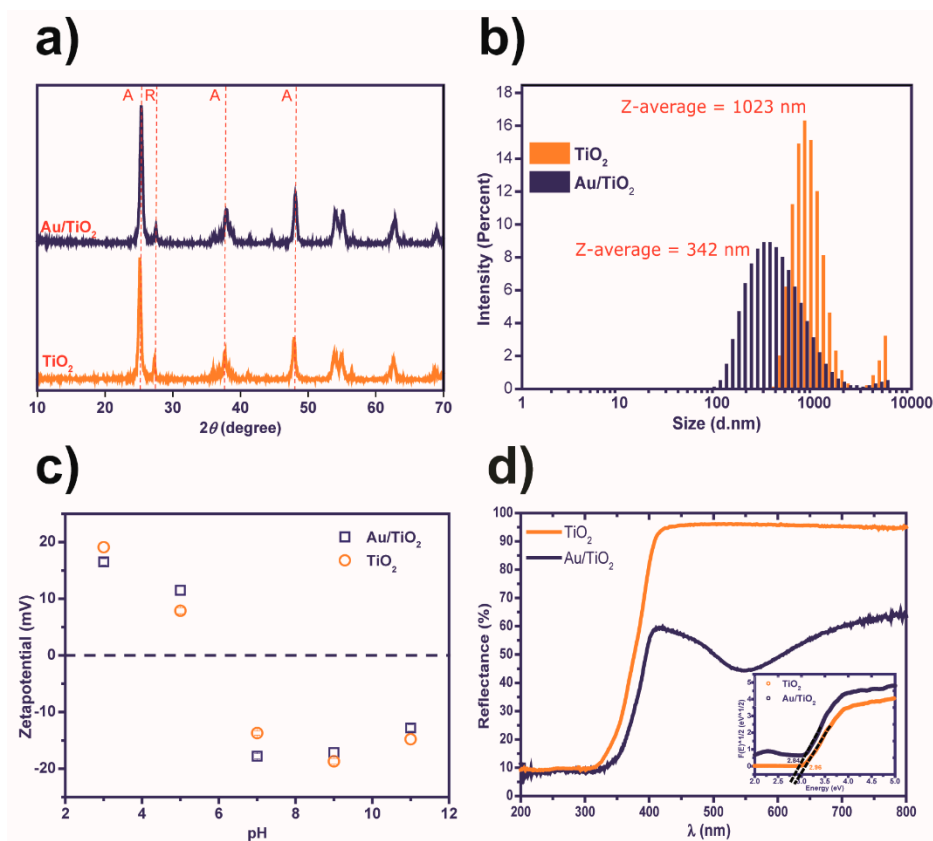
Figure 4. X-ray diffraction reflexes of pristine TiO_2 and Au/TiO_2 nanocomposite and identification of the representative peaks for anatase (A) and rutile (R) phases (**a**); dynamic light scattering, intensity size distribution of the pristine TiO_2 and the Au/TiO_2 nanocomposite and respective Z-average hydrodynamic size (**b**); zeta potential measurements, performed at different pHs (3, 5, 7, 9, and 11) for pristine TiO_2 nanoparticles and Au/TiO_2 nanocomposite (**c**); UV–vis reflectance spectra of pristine TiO_2 and Au/TiO_2 and (inset) the estimation of the bandgap for both samples at $(F(R))1/2 = 0$ (**d**). The Au/TiO_2 nanocomposite synthesized at 60 °C and with an Au loading of 0.05 wt. % was used.

To understand the differences in the photocatalytic performance of TiO_2 and Au/TiO_2 nanocomposite, the optical properties of these materials were studied by UV-visible diffuse reflectance spectra (DRS), depicted in Figure 4d. In the visible range (400–800 nm), the pure TiO_2 nanoparticles reflect the radiation almost entirely ($\approx$ 95%). However, the nanocomposite displays reflectance below 64% for the same range. Additionally, a minimum reflectance ($\approx$ 44%) was obtained at 545 nm, indicating a maximum of absorbance band that can be associated with the surface plasmon of Au nanoparticles, typically in the wavelength range between 520 and 560 nm [47,48]. These results show that the nanocomposite presented a broad absorbance spectrum when compared to the pristine TiO_2 nanoparticles, which is also consistent with the purple/pink color exhibited by the produced nanocomposite. In the ultraviolet range (200–400 nm), both samples showed similar behavior.

From DRS spectra it was possible to estimate the band gap, shown in the inset graph of Figure 4d, for pure TiO_2 and Au/TiO_2 nanocomposite was converting the reflectance to Kubelka–Munk units through Equation (1) and Equation (2). The obtained values show that the nanocomposites possessed a lower bandgap (2.84 eV) than the pristine TiO_2 nanoparticles (2.96 eV). The decrease of the bandgap in Au/TiO_2 was related to the shift absorption to longer wavelengths. Similar results have been reported in the literature [49,50].

### 2.2. Nanocomposites' Optimization and Photocatalytic Experiments

The photocatalytic activity of all the produced Au/TiO$_2$ nanocomposites was assessed by monitoring the degradation of CIP under artificial UV and visible irradiations. Process conditions were varied depending on the studying purposes.

Nanocomposite Optimization

As gold is a noble metal, cost-effectiveness should be considered, and the amount of gold used in the nanocomposite is one of the most paramount parameters. In this study, Au loading was varied by using different concentrations of the gold precursor. The tested Au loadings were 0.025, 0.05, 0.1, 0.25, and 0.5 wt. %. These nanocomposites were employed for the photocatalytic degradation of CIP under both UV and simulated visible radiation.

Figure 5a shows the data of photocatalytic experiments under UV light. Accordingly, all produced samples and the pristine TiO$_2$ used as a control showed photocatalytic activity, proven by the decrease of CIP concentration along with the irradiation time. As confirmed by the diffuse reflectance spectroscopy (Section 2.1), the bandgap of the nanocomposites was 2.84 eV, corresponding to the wavelength of 437 nm. Here, the used UV lamp had the mode wavelength of 365 nm, which was shorter than the bandgap. It means that the photon energy was adequate to excite the photocatalytic materials, and photocatalytic reaction occurred in all experiments. Pristine TiO$_2$ was compared with the synthesized photocatalysts. After 30 min, 77% of CIP was degraded in the presence of pristine TiO$_2$, whereas higher degradation of 80–90% was achieved in the same time of irradiation, using the synthesized photocatalysts, 0.05 wt. %. This efficiency can be assigned to the presence of gold particles on the surface of the photocatalysts, confirmed by the TEM and EDX characterization (Section 2.1). The further quantitative inspection was obtained using the Langmuir–Hinshelwood kinetics (Equation (3)), and data are shown in Table 1. The apparent reaction rate constant k of the experiment with the bare TiO$_2$ was found to be 0.047 min^{-1}, while the decoration with gold particles improved the photocatalytic activity by 2–3 times. As predicted, in the presence of gold, the excited electrons may be conducted to the gold particles, and the electron-hole recombination may be reduced, which prolongs the lifetime of generated holes [51,52].

Consequently, the photocatalytic activity of the composites increased. Additionally, the increase of the used chloroauric acid concentration might induce a more significant number of gold particles distributed on the TiO$_2$ surface. In other words, the number of electron absorption centers was increased, which explains the increase of k from 0.078 to 0.131 min^{-1} when increasing the Au loading from 0.025 to 0.5 wt. %. However, the further increase in the Au loading caused a decrease in k. These results can be addressed to the loss of photocatalytic active sites on the surface of TiO$_2$ nanoparticles. Based on the TEM images shown in Figure 1, when the Au loading was very high both the amount and the size of Au nanoparticles over the surface of TiO$_2$ nanoparticles were larger, which contributed to a reduction of the adsorption and probably to mitigate the radiation absorbance by the catalytic nanoparticles. Together, these limitations contributed to reducing the photocatalytic efficiency of the nanocomposite towards the samples with lower amounts of Au and demonstrated the relevance of optimizing the Au loading.
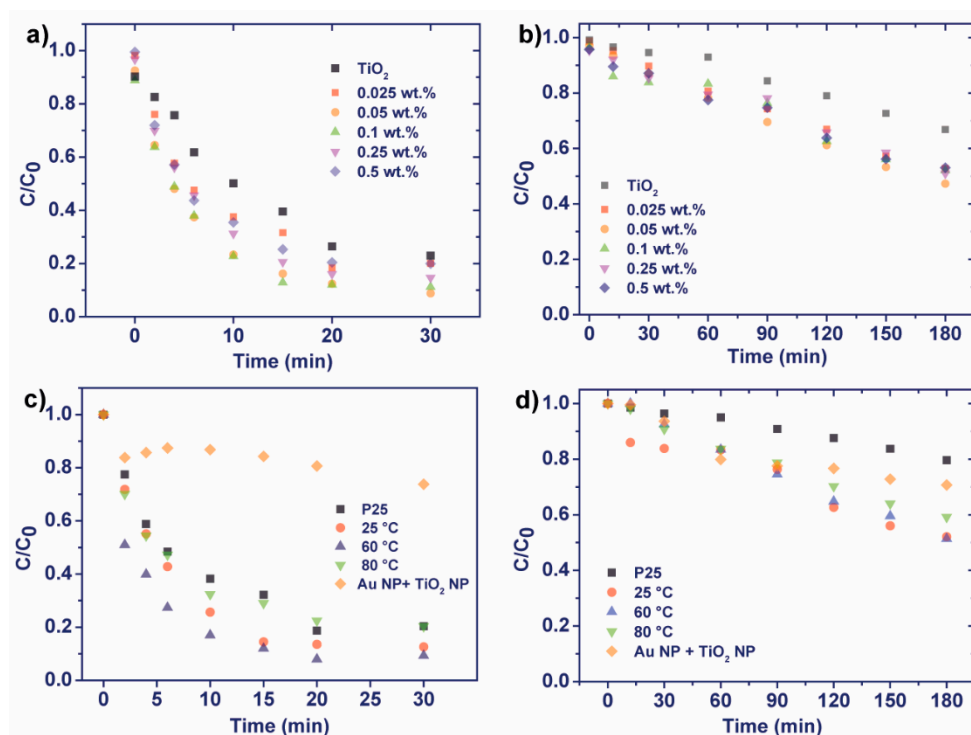
Figure 5. Photocatalytic degradation of ciprofloxacin (5 mg/L) with bare TiO_2 and Au/TiO_2 nanocomposite with different Au concentrations under 30 and 180 minutes of UV (**a**) and visible (**b**) radiation. The degradation with bare TiO_2 and Au/TiO_2 nanocomposites synthesized at different temperatures and Au loading of 0.05 wt. % under 30 and 180 minutes of UV (**c**) and simulated visible light radiation (**d**), respectively.

Table 1. Apparent reaction rates (k) for photocatalytic degradation of ciprofloxacin (CIP) (5 mg/L) with bare TiO_2 and Au/TiO_2 nanocomposite with different Au loadings, over 30 and 180 minutes of UV and simulated visible radiation, respectively.

Au loading (wt. %)	UV k (min^{-1})	Simulated Visible k (h^{-1})
0	0.047	0.073
0.025	0.078	0.211
0.05	0.099	0.242
0.1	0.131	0.211
0.25	0.089	0.195
0.5	0.076	0.202

The photocatalytic assays performed under visible illumination are shown in Figure 6b. Regarding these assays, it is essential first to mention the controls (Supplementary Material, Figures S3 and S4), which have shown that the CIP solution was stable under simulated visible radiation, demonstrating its photostability. Moreover, another control was performed by adding the Au/TiO_2 nanocomposites to CIP solution in the dark for 180 minutes. In this case, approximately 11% of CIP was removed from the solution by adsorption to the Au/TiO_2 nanocomposites.
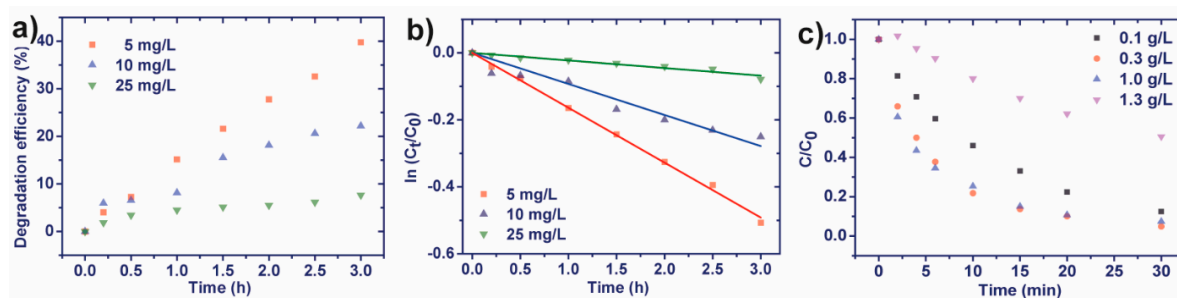
Figure 6. Degradation efficiency (%) (**a**) and ln (C/C0) vs. time (**b**) for different initial ciprofloxacin concentrations (5, 10, and 25 mg/L), using Au/TiO$_2$ nanocomposites produced at 60 °C and with an Au loading of 0.05 wt. %, under 3 hours of simulated visible radiation. Photocatalytic degradation of ciprofloxacin (5 mg/L) in 45 mL of aqueous solution with different Au/TiO$_2$ concentrations (0.1, 0.3, 1.0, and 1.3 g/L). The Au/TiO$_2$ nanocomposite synthesized at 60 °C and with an Au loading of 0.05 wt. % was used. The tests were performed over 30 minutes under UV irradiation (**c**).

With the information from controls, it is possible to understand the photocatalytic efficiency of the tested materials better. Similarly, to the UV light experiments, the degradation rates of all produced nanocomposites were faster than that with the bare TiO$_2$. TiO$_2$ could remove $\approx$ 33% of CIP after 180 min of simulated visible irradiation. This CIP removal may be assigned to adsorption, confirmed by controls performed in the dark (as above mentioned). Additionally, the sun simulator device had a small percentage ($\approx$ 3%) of UV radiation (to mimic sunlight radiation). This radiation can induce a low photocatalytic activity on bare TiO$_2$, which, together with the adsorption of CIP, is responsible for its removal from the solution.

More importantly, the decoration of gold particles on the TiO$_2$ surface resulted in the faster degradation rate of CIP under visible radiation. The bandgap of the composites was lowered, from 2.96 eV to 2.84 eV (Section 2.1). Similar results were obtained for methylene blue degradation using Au/TiO$_2$ nanoparticles. The authors obtained higher degradation efficiencies and ability to use visible radiation [37]. Thus, the materials could absorb the longer wavelength in the visible range (up to 437 nm). The reaction rates' constant increased from 0.073 h^{-1}, without Au, to 0.195–0.224 h^{-1}, with different Au loadings (Table 1).

The obtained results, for UV and visible radiation, confirmed that the photocatalytic efficiency of the TiO$_2$ nanoparticles was enhanced with the Au loading, until a specific plateau. When the Au loading was higher than 0.1 and 0.05 wt. %, respectively, for UV and visible radiation, the gold nanoparticles can block the surface-active sites of TiO$_2$ nanoparticles [53,54]. Furthermore, an excessive amount of Au nanoparticles can play as recombination centers for photo-induced electrons and holes. Both situations can contribute to a significant reduction of pollutant adsorption and, consequently, the photocatalytic efficiency [55]. The remaining assays of this study will be performed with an Au loading of 0.05 wt. %.

Another critical parameter that is worth to stress and study is temperature, which can affect the surface charge phenomenon and the dispersity of the TiO$_2$ particles in the solution during the synthesis. It can also influence the nucleation and the gold particles' crystal growth on the TiO$_2$ nanoparticle surface. In this study, the synthesis was operated at 25, 60, and 80 °C, and the photocatalytic degradation of CIP, with the nanocomposites produced at different temperatures, was performed under UV and visible radiation (Figure 5c,d and Table 2). Regardless of the synthesis temperature, the photocatalytic activity of the nanocomposites (Au loading = 0.05 wt. %) was equal or higher than that of the bare TiO$_2$. Here, the synthesis at the room and medium temperatures (25 and 60 °C) yielded the more efficient photocatalytic materials, for UV and visible radiation, towards higher temperature synthesis (80 °C).

Table 2. Apparent reaction rates (k) for photocatalytic degradation of CIP (5 mg/L) with bare TiO_2 and Au/TiO_2 nanocomposite synthesized at different temperatures, over 30 and 180 minutes of UV and simulated visible radiation, respectively. The Au loading of 0.05 wt. % was used for the tested materials.

Temperature (°C)	UV		Simulated Visible	
	k (min^{-1})	Degradation (%)	k (h^{-1})	Degradation (%)
TiO_2	0.66	80	0.073	20
25	0.131	88	0.221	48
60	0.117	91	0.226	49
80	0.047	80	0.176	41

For both types of radiation, the sample obtained at 60 °C presented higher degradation efficiencies (Table 2), 91% and 49% of CIP degradation under UV (30 min) and visible radiation (180 min), respectively. On the other hand, the synthesis performed at 80 °C revealed lower degradations rates of 80% and 40% for UV and visible radiation, respectively. Other works have reported that higher temperatures accelerate the reduction process and yield broader Au nanoparticles size distributions [56].

In this context, when the synthesis occurred at 80 °C, the size of Au nanoparticles produced was larger than the sizes obtained with 25 °C and 60 °C (in good agreement with STEM-HAADF micrographs, Figure 1). Similarly to what happened with the Au loading, when the amount of Au on the surface of TiO_2 was too high, the active sites were blocked and the pollutant adsorption can be limited. Compared with bare TiO_2, these results corresponded to a degradation efficiency increase of approximately 13% and 145% for UV and visible radiation, respectively.

Both under UV and visible radiation, another control was performed (Figure 5c,d) by testing single Au nanoparticles at the very same amount of Au (corresponding to 0.05 wt. % obtained at 60 °C) and TiO_2 nanoparticles on CIP degradation. The results confirmed that the photocatalytic efficiency obtained by the nanocomposites should be assigned to the interface between Au and the TiO_2 surface.

2.3. Photocatalytic Degradation

The rate of photocatalytic degradation depends on the availability of the catalyst surface for the photo-generation of electron-hole pairs that produce hydroxyl radicals. Thus, in these experiments, the amount of catalyst was kept constant, and the number of hydroxyl radicals generated remained the same, while CIP concentration increased. The influence of CIP initial concentration of 5, 10, and 25 mg/L was studied under visible irradiation. It was observed that the CIP concentration impacted by the degradation rate and efficiency (Figure 6). With the lowest CIP concentration, 40% of CIP degradation was obtained after 30 min. With the increase of concentrations by 2 and 5 times, the efficiencies achieved were 22% and 8%, respectively. In these tests, while using the photocatalyst concentration of 0.3 g/L, the adsorption of the CIP on the Au/TiO_2 nanoparticles surface might be halted due to surface saturation. Additionally, the presence of organic compounds such as CIP can generate an increased number of intermediates and products, which will compete with CIP for adsorption on the photocatalyst surface [57]. This competition caused a lower reaction rate for high CIP concentration. The following assays, focused on the photocatalytic activity of the produced nanocomposites, were performed using the lowest CIP concentration, 5 mg/L.

In short, the ratio between hydroxyl radical/CIP molecules decreased with higher concentrations, causing lower photocatalytic activity. Moreover, higher CIP concentrations may also reduce radiation harvesting by TiO_2 nanoparticles surface, which will also contribute to decreasing the number of hydroxyl radicals formed. Figure 6b displays the plot of ln (C/C0) vs. time at different initial CIP concentrations. Linear plots were observed, and the R^2 values were higher than 0.9, confirming that the photocatalytic degradation of CIP obeyed pseudo first-order kinetics.

The optimal photocatalyst concentration was assessed through degradation of CIP with the different amounts of Au/TiO_2 nanocomposites, from 5 to 60 mg, which corresponded to a photocatalyst concentration of 0.1 and 1.3 g/L, respectively. Experimental results are shown in Figure 6c.

In general, with the photocatalytic concentrations of 0.1–1.0 g/L, $\approx$ 90% of the CIP in solution was degraded, while with the higher concentration of 1.3 g/L, only 50% CIP was degraded after exposure to the same UV irradiation time. At the lowest photocatalytic concentrations of 0.1–0.3 g/L, the photocatalytic degradation increased significantly with the amount of nanocomposite. Indeed, the increased amount of photocatalyst resulted in higher surface coverage, owing to the highest number of active sites [58]. However, when increasing the concentration to 1.0 g/L, the degradation rate remained unchanged. With the highest concentration of Au/TiO2, 1.3 g/L, the degradation was slowest likely because of excessive turbidity that induced light extinguishment after penetrating a short distance from the illuminated surface [59]. Most of the light might be extinguished after penetrating a short distance from the illuminated surface of the suspension. Thus, photocatalytic particles in an inner region could not be activated. The result agrees with other reports [58,60]. For this reason, the concentration of 0.3 g/L (15 mg in 45 mL), which yielded the highest photocatalytic efficiency, was chosen for the following photocatalytic activity assays.

The reproducibility of the nanocomposites efficiency was also tested using three independent syntheses, performed under the same conditions. The produced samples were then used in the photocatalytic degradation of CIP under visible radiation (results in the Supplementary Material, Figure S5). The apparent reaction rate constant of the three experiments fluctuated around the value of 0.219 ± 0.022 min^{-1}. The standard deviation of 10% proved the reproducibility of the method to enhance the photocatalytic activity of pure TiO_2 nanoparticles and endow them with visible light activity. It is also important to clarify that the Au concentrations used in this study were nominal, as no inductively coupled plasma atomic emission spectroscopy (ICP-AES), or similar characterization, was performed. However, given the considerable reproducibility of the method, the putative loss of gold would by similar for all the Au concentrations tested, making them comparable.

## 3. Computational Modeling: Gold on Titanium Dioxide and Charge Transfer

A computational study was performed to rationalize the effect of gold nanoparticles on TiO_2. The GFN-xTB (Geometry, Frequency, Noncovalent, eXtended Tight-Binding) was used. GFN-xTB is a new semiempirical method developed by Grimme et al. [61] that allows computing efficiently systems with thousands of atoms. The GFN-xTB software used (version 5.4.6) did not allow us to compute systems with periodic boundary conditions, so a finite system composed of a gold nanoparticle adsorbed on a larger TiO_2 nanoparticle was used. We chose a cuboctahedral $(TiO_2)_{97}$ anatase nanoparticle, which was found to produce bulk-like electronic properties [62] and had two large, equal, flat surfaces of $\sim 1.2 \times 1.5$ nm^2 on which a cuboctahedral $(Au_{55})^{-3}$, 10 nm diameter, gold nanoparticle was adsorbed [63]. Several adsorption modes were possible, yet an exhaustive search of these was beyond the scope of this study. We positioned the gold nanoparticle on four, arbitrary, different orientations so that, in all cases, one of the faces of $(Au_{55})^{-3}$ was parallel to the anatase flat surface and minimized. In this minimization, the TiO2 coordinates were held fixed while the Au first neighbors' distances were constrained harmonically to an equilibrium value to force the gold nanoparticle to keep its initial shape while retaining some flexibility. Two different pH conditions were considered: (1) A neutral/basic pH represented by the bare $(TiO_2)_{97}$ anatase nanoparticles (i.e., without protonation), and (2) an acidic pH, where the eight under-coordinated oxygen atoms in the anatase nanoparticle were protonated, $(TiO_2)_{97}H_8^{+8}$, which should represent better the experimental conditions (Figure 7).
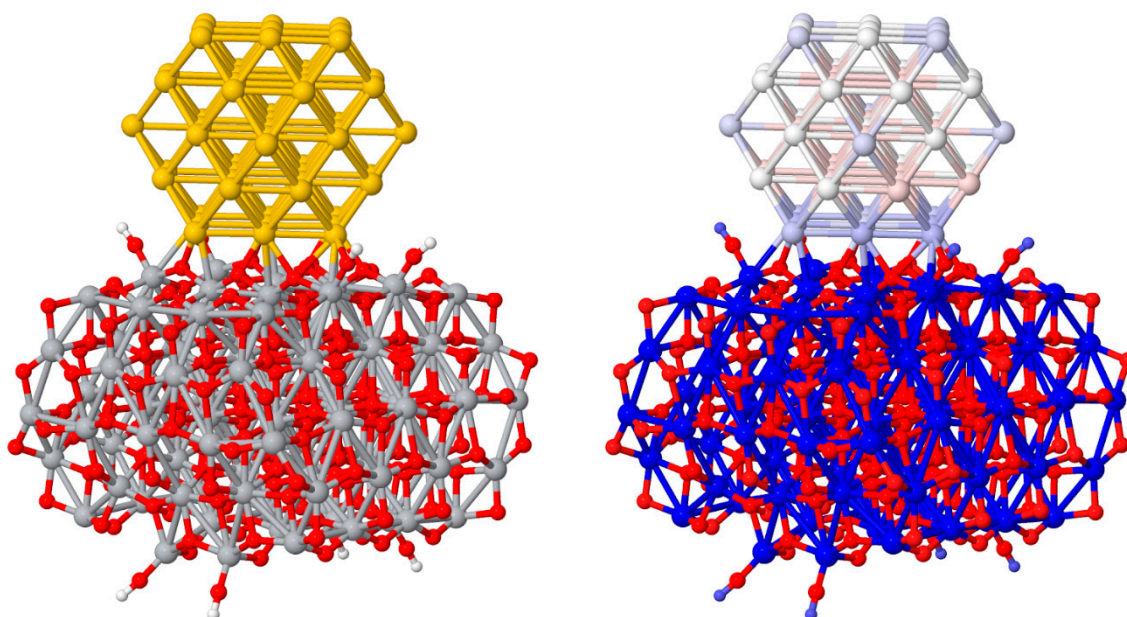
Figure 7. The $(Au_{55}(TiO_2)_{97}H_8)^{+5}$ with standard atom coloring (left) with color-rendered atomic charges (right), so that red represents negatively charged atoms, blue positively charged atoms, and white neutral atoms.

To study the charge transfer between $(Au_{55})^{-3}$ and $(TiO_2)_{97}$ and $((TiO_2)_{97}H_8)^{+8}$, we computed atomic charges specifically suited for condensed phases [64]. The analysis of the charges in $(Au_{55}(TiO_2)_{97})^{-3}$ and $(Au_{55}(TiO_2)_{97}H_8)^{+5}$ (Figure 7) show that the Au nanoparticle transferred electrons to the anatase, namely 4.7 electrons for neutral TiO_2 and 4.3 electrons for the protonated TiO_2. Most of this charge was transferred directly to Ti atoms, namely 3 and 3.3 electrons for the neutral and protonated case, respectively. So, the Au acted as an electron donor populating the Ti(d) states that were responsible for the photocatalytic activity of the material. Consequently, Au may increase the catalytic activity of the composite material through interfacial electron transfer. Interestingly, the anatase surface also polarized the gold nanoparticle so that all atoms in direct contact with TiO_2 were more oxidized, i.e., had larger positive charges, see Figures 7 and 8.

This effect was observed in all cases, for neutral and acidic pH and when the harmonic constraint on Au atoms was released, which indicates that the observed charge transfer is a fundamental process of the Au-TiO_2 interface. This corroborated the experimental controls shown in Figure 5c,d, showing that separation of Au and TiO_2 nanoparticles yielded lower efficiencies. Moreover, this finding also fit previous DFT (density functional theory) calculations which found that an Au nanorod on a rutile TiO_2 (110) surface might act as an activator for molecular oxygen through charge transfer to nearby Ti^{+4} atoms [65]. Mechanistically, the presence of Au activated superficial Ti^{+4} atoms nearby for catalysis via direct charge transfer, which rationalized our experimental observation that lower Au loading and small gold nanoparticles had larger catalytic activity than larger loadings and nanoparticles on TiO_2.
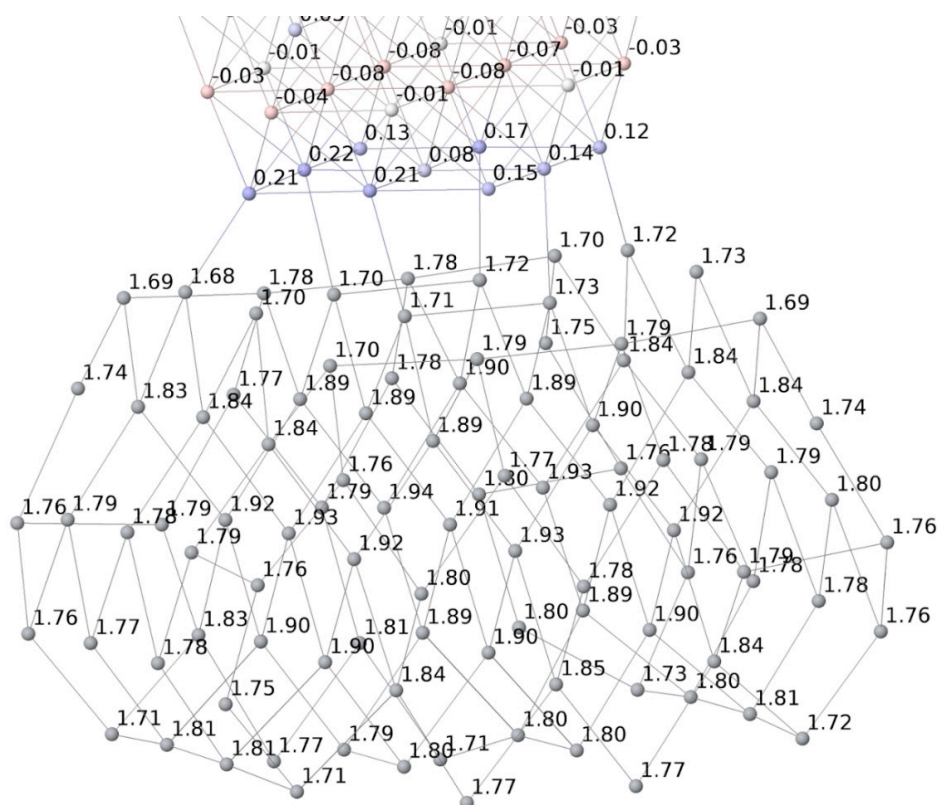
Figure 8. The $(Au_{55}(TiO_2)_{97}H_8)^{+5}$ with only the titanium subnetwork and gold atoms with their corresponding point charges.

Adsorption of Ciprofloxacin on $Au_{55}(TiO_2)_{97}H_8{}^{+58}$

We also explored the different energetics of a CIP molecule interacting with $(Au_{55}(TiO_2)_{97}H_8)^{+58}$ on four different adsorption sites (Figure 9). All the adsorption modes were found to be binding, i.e., exothermic, with energies ranging between 0.7 and 2.4 eV. The strongest binding was observed for the structure with a large contact between the oxygen atom of the carboxylic group and the gold nanoparticle, 2.4 eV. This binding was similar in energy to the adsorption on the anatase clean surface (2.1 eV), which indicates that both processes might be competitive and that CIP molecules might also adsorb near the gold/anatase interface where the Ti atoms were activated through electron transfer.

| 2.1 eV | 2.4 eV | 0.7 eV | 1.5 eV |
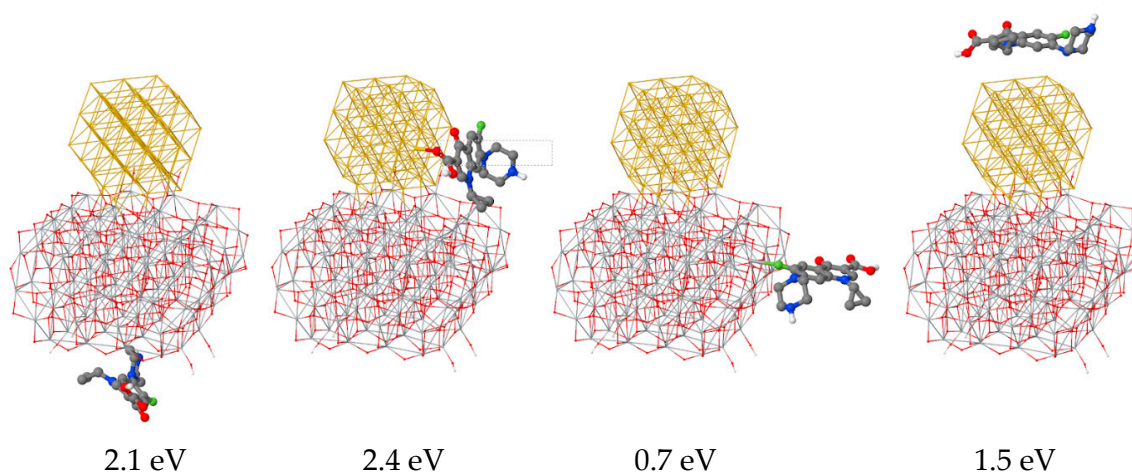
Figure 9. Four possible adsorption geometries of CIP on $(Au_{55}(TiO_2)_{97}H_8)^{+58}$ with corresponding binding energies. The positive binding energies indicate that the process is exothermic.

4. Materials and Methods

4.1. Materials

P25 TiO$_2$ nanoparticles were kindly provided by Evonik (Essen, Alemanha). Gold(III) chloride trihydrate, 99.9% CAS: 16961-25-4 (liquid solution) was purchased from Sigma-Aldrich (St. Louis, Missouri, EUA). Sodium hydroxide (NaOH) was obtained from VWR (Radnor, Pensilvânia, EUA) Millipore Milli-Q-system ultra-pure (UP) water was used in all the experiments.

4.2. Nanocomposite Synthesis

The Au/TiO$_2$ nanocomposites were synthesized, as illustrated in Figure 10, dispersing 200 mg of TiO$_2$-P25 nanoparticles in 40 mL of ultra-pure (UP) water in a sonication bath for 30 min. Afterwards, this solution was placed under agitation in a water bath at different temperatures (25, 60, and 80 °C), using a thermostat to precisely control and stabilize the temperature, avoiding thermal gradients. When the dispersion solution reached the desired temperature, different volumes from the chloroauric solution (10 μL of Gold(III) chloride trihydrate in 100 mL of UP water) were added to achieve the Au loadings of 0.025, 0.05. 0.1, 0.25, and 0.5 wt. %. The solution was then stirred for 10 minutes to achieve a homogeneous distribution of gold precursor solution. Later, several volumes of a 0.1 M sodium hydroxide solution (NaOH) were added dropwise and mixed for 10 minutes to obtain a pH = 9. The solution was then centrifuged at 23,000 rpm, the supernatant discarded, and the nanocomposite pellet redispersed in UP water with the ultrasonication for 1 minute, and this washing procedure was repeated one more time. The last step was to dry the nanocomposite at 80 °C in an oven overnight and grind it with a pestle and mortar to obtain a fine powder.
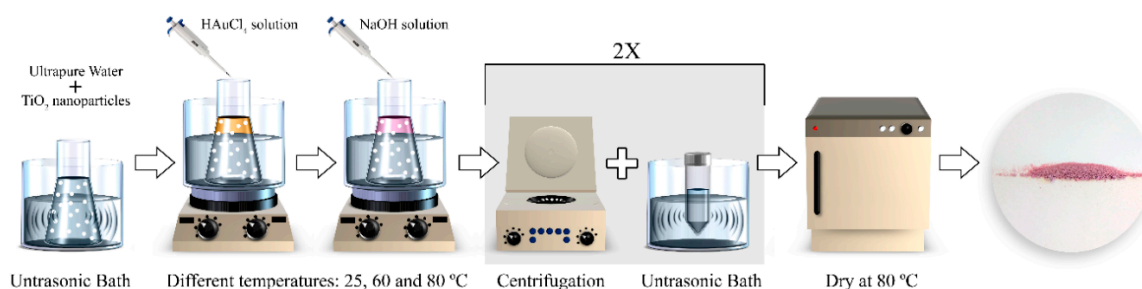
Figure 10. Schematic representation of the main steps to synthesize Au/TiO$_2$ nanocomposites trough nanoprecipitation.

4.3. Characterization

The morphology of the nanocomposites was assessed by transmission electron microscopy (TEM), a Tecnai T20 from FEI (Hillsboro, Oregon, EUA). For the analysis, the nanocomposite samples were sonicated for 5 minutes to achieve good dispersion and afterwards a drop of the suspension was placed on a copper grid and dried at room temperature for the analysis. Particle size histograms were obtained after measuring at least 200 nanoparticles using Image J 1.50i software. Aberration-corrected scanning transmission electron microscopy (Cs-corrected STEM) images were acquired using a high-angle annular dark field detector in an FEI XFEG TITAN (Hillsboro, Oregon, EUA) electron microscope operated at 300 kV equipped with a Spherical Aberration Corrector for Transmission Electron Microscopes (CETCOR) Cs-probe corrector from CEOS Company (Heidelberg, Germany), allowing the formation of an electron probe of 0.08 nm. Elemental analysis was carried out with an EDX (energy-dispersive X-ray spectroscopy) detector, which allows performing EDX experiments in the scanning mode.

The crystallographic phases of the pure TiO$_2$ and the Au/TiO$_2$ nanocomposite were evaluated by X-ray diffraction using a D8 Discover diffractometer with incident Cu Kα (40 kV and 30 mA), from Bruker (Billerica, Massachusetts, EUA).

The average hydrodynamic diameter was assessed by dynamic light scattering (DLS) in a Zetasizer NANO ZS-ZEN3600, Malvern (Malvern Instruments Limited, United Kingdom), equipped with a He–Ne laser (wavelength 633 nm) and backscatter detection (173°). The samples were dispersed (0.1 mg/L) in ultrasonication bath at 22 °C for 30 minutes to avoid aggregates, and each sample was measured 10 times. The zeta (ζ) potential was measured in the same device, and TiO_2 nanoparticles were equally suspended in ultra-pure water and solutions at different pHs (2, 4, 7, 9, and 12) were prepared with HCl (1M) and NaOH (1M) solutions. The results were obtained using the Smoluchowski theory approximation, and each sample was measured 10 times at 22 °C. The manufacturer software (Zetasizer 7.12) was used to assess particles diameter (intensity distribution), the polydispersity index (PDI), and z-potential values.

The optical properties of the pristine TiO_2 and the Au/TiO_2 nanocomposite were assessed by UV–vis reflectance, using a Shimadzu UV-2501-PC (Kyoto, Japan) equipped with an integrating sphere. The spectra were acquired in reflectance, and the bandgap was estimated via the Kubelka–Munk Equation (1) [52] and the Tauc plot represented by Equation (2).

$$F(R) = (1 - R_\infty)^2 / (2R_\infty) \tag{1}$$

where R_∞ ($R_{\text{Sample}}/R_{\text{BaSO4}}$) corresponds to the reflectance of the sample and $F(R)$ is the absorbance.

$$[F(R)h\upsilon]^{1/n} \text{ versus } h\upsilon \tag{2}$$

where h is the Planck constant (6.626×10^{-19} J), n is the frequency, and n is the sample transition (indirect transition, $n = 2$) [66].

4.4. Photocatalytic Degradation

The photocatalytic activity of all the produced samples and pristine TiO_2 was assessed by performing (CIP) degradation tests, under artificial ultraviolet (UV) or visible illumination. First, a solution of 5 mg/L of CIP was prepared. The CIP solution was adjusted to pH = 3, to ensure the solubility, by using 0.1 mL hydrochloric acid (HCl) 1 M.

Before the degradation assays (UV or visible radiation), the Au/TiO_2 or P25 nanoparticles were stirred in the dark for 30 min to achieve an adsorption-desorption equilibrium.

The UV degradation of CIP was performed in a chamber with six Philips 8 W mercury fluorescent lamps with the mode wavelength of 365 nm. The suspensions of photocatalysts and CIP were kept stirred in a container under the illumination from the top. The distance between the beaker and the lamp was 13.5 cm, and the intensity coming to the system was 15–17 W/m^2. The samples were irradiated for 30 min.

The visible light tests were performed in a visible chamber fabricated by Ingenieurbüro Mencke & Tegtmeyer GmbH©, Hameln, Alemanha. According to the manufacturer, the visible light spectrum was equivalent to that of the natural solar light. The light source had an intensity of 98 W/m^2. The visible light test was performed similarly to the UV test. Here, the container was placed at 21 cm from the light source, and the samples were irradiated continuously for 180 minutes.

The first photocatalytic activity tests were performed to determine the optimal ratio of CIP/catalyst. For this purpose, 5, 15, 45, and 60 mg of Au/TiO_2 nanocomposite were dispersed in a borosilicate beaker of 80 mL with 45 mL of CIP solution (5 mg/L). The effect of Au loading on the photocatalytic efficiency was also assessed, under UV and simulated visible radiation. The impact of the synthesis temperature (25, 60, and 80 °C) on CIP photocatalytic degradation was equally evaluated using both types of illumination. The photocatalytic reproducibility tests were performed using nanocomposites produced in different batches but under the same synthesis conditions.

The bare TiO_2 nanoparticles were used as controls in all the assays. Additionally, to prove the relevance of the Au/TiO_2 nanocomposites' structure and interface, the photocatalytic degradation of

CIP was assessed using the same amounts of Au and TiO$_2$ nanoparticles, not as a nanocomposite, but separately added to the solution.

The photocatalytic efficiencies were tested by degrading CIP in aqueous solution under UV and visible radiation and monitoring the maximum absorption peak (277 nm) using a Shimadzu UV-2501PC UV/Vis spectrophotometer. The degradation fit the Langmuir-Hinshelwood model, expressed by Equation (3):

$$C/C_0 = exp^{-kt} \tag{3}$$

where C_0 and C represent the concentration of the pollutant at time 0 min and at time t, respectively, and k is the first-order rate constant of the reaction.

5. Conclusions

An Au/TiO$_2$ nanocomposite was produced, characterized, and applied in the photocatalytic degradation of ciprofloxacin (CIP). The characterization results changing the synthesis conditions (temperature and Au loading) indicated that the synthesis performed at 60 °C with the Au loading of 0.05 wt. % yielded the most homogeneous distribution of Au nanoparticles ($\approx$3 nm) over TiO$_2$ nanoparticles surface, after TEM inspection. Additionally, these samples absorbed more radiation in the visible range ($\approx$66% at 545 nm) and presented a lower bandgap (2.84 eV vs. 2.96 eV from bare TiO$_2$). The photocatalytic results confirmed that all the manufactured nanocomposites possessed higher photocatalytic efficiency in the UV and simulated visible radiation towards the pristine TiO$_2$. It was also possible to understand the impact of the synthesis parameters envisaging the optimal photocatalytic efficiency conditions. In this way, with the Au/TiO$_2$ nanocomposite, it was possible to enhance the photocatalytic degradation efficiency in 13% and 145% under UV and simulated visible light radiation, respectively. The gold nanoislands played a paramount role transferring electrons from Au to the anatase from TiO$_2$ nanoparticles. Additionally, Au endowed the nanocomposite with the ability to absorb the visible radiation.

Computational modeling supported the experimental data, showing the ability of Au to bind TiO$_2$ anatase surfaces as well as the relevant role of Au transferring electrons. The fundamental importance of the interface between TiO$_2$ and Au nanoparticles regarding the enhanced photocatalytic activity was also rationalized. Moreover, models indicated a high affinity of CIP to both Au and TiO$_2$ surfaces, which favors the adsorption process and consequently may also be cause for enhanced photocatalytic efficiency in the presence of Au nanoparticles.

According to the results obtained through systematic experimental data and modeling results, the simple method herein presented constitutes a reliable approach to produce efficient photocatalytic materials.

Author Contributions: Conceptualization, P.M. and S.L.-M.; data curation, P.M., S.K., and H.N.L.; formal analysis, H.N.L., L.P., M.M.-F., and S.L.-M.; investigation, P.M., S.K., H.N.L., and M.M.-F.; methodology, P.M., S.K., and V.S.; project administration, S.L.-M.; resources, V.S., M.A., G.C., and S.L.-M.; software, M.M.-F.; supervision, K.K., M.A., G.C., and S.L.-M.; validation, V.S.; visualization, P.M. and M.M.-F.; writing—original draft, P.M. and H.N.L.; writing—review & editing, P.M., M.A., and S.L.-M. All authors have read and agreed to the published version of the manuscript.

Conflicts of Interest: The authors declare no conflict of interest.

References

1. An, T.; Yang, H.; Song, W.; Li, G.; Luo, H.; Cooper, W.J. Mechanistic considerations for the advanced oxidation treatment of fluoroquinolone pharmaceutical compounds using TiO_2 heterogeneous catalysis. *J. Phys. Chem. A* **2010**, *114*, 2569–2575. [CrossRef]

2. Li, W.C. Occurrence, sources, and fate of pharmaceuticals in aquatic environment and soil. *Environ. Pollut.* **2014**, *187*, 193–201. [CrossRef]

3. Ayati, A.; Ahmadpour, A.; Bamoharram, F.F.; Tanhaei, B.; Mänttäri, M.; Sillanpää, M. A review on catalytic applications of Au/TiO_2 nanoparticles in the removal of water pollutant. *Chemosphere* **2014**, *107*, 163–174. [CrossRef] [PubMed]

4. Jiang, J.-Q.; Ashekuzzaman, S.M. Development of novel inorganic adsorbent for water treatment. *Curr. Opin. Chem. Eng.* **2012**, *1*, 191–199. [CrossRef]

5. Kumar, S.; Ahlawat, W.; Bhanjana, G.; Heydarifard, S.; Nazhad, M.M.; Dilbaghi, N. Nanotechnology-based water treatment strategies. *J. Nanosci. Nanotechnol.* **2014**, *14*, 1838–1858. [CrossRef] [PubMed]

6. Pawar, R.C.; Lee, C.S. *Heterogeneous Nanocomposite-Photocatalysis for Water Purification*; William Andrew: London, UK, 2015.

7. Lu, S.-Y.; Wu, D.; Wang, Q.-L.; Yan, J.; Buekens, A.G.; Cen, K.-F. Photocatalytic decomposition on nano-TiO_2: Destruction of chloroaromatic compounds. *Chemosphere* **2011**, *82*, 1215–1224. [CrossRef]

8. Khaki, M.R.D.; Shafeeyan, M.S.; Raman, A.A.A.; Daud, W.M.A.W. Application of doped photocatalysts for organic pollutant degradation—A review. *J. Environ. Manag.* **2017**, *198*, 78–94. [CrossRef]

9. Fabregat-Santiago, F.; Barea, E.M.; Bisquert, J.; Mor, G.K.; Shankar, K.; Grimes, C.A. High carrier density and capacitance in TiO_2 nanotube arrays induced by electrochemical doping. *J. Am. Chem. Soc.* **2008**, *130*, 11312–11316. [CrossRef]

10. Hoffmann, M.R.; Martin, S.T.; Choi, W.; Bahnemann, D.W. Environmental applications of semiconductor photocatalysis. *Chem. Rev.* **1995**, *95*, 69–96. [CrossRef]

11. Vargas Hernández, J.; Coste, S.; García Murillo, A.; Carrillo Romo, F.; Kassiba, A. Effects of metal doping (Cu, Ag, Eu) on the electronic and optical behavior of nanostructured TiO_2. *J. Alloy. Compd.* **2017**, *710*, 355–363. [CrossRef]

12. Shen, L.; Liang, R.; Wu, L. Strategies for engineering metal-organic frameworks as efficient photocatalysts. *Chin. J. Catal.* **2015**, *36*, 2071–2088. [CrossRef]

13. Ahmad, R.; Ahmad, Z.; Khan, A.U.; Mastoi, N.R.; Aslam, M.; Kim, J. Photocatalytic systems as an advanced environmental remediation: Recent developments, limitations and new avenues for applications. *J. Environ. Chem. Eng.* **2016**, *4*, 4143–4164. [CrossRef]

14. Carneiro, J.T.; Yang, C.-C.; Moma, J.A.; Moulijn, J.A.; Mul, G. How gold deposition affects anatase performance in the photo-catalytic oxidation of cyclohexane. *Catal. Lett.* **2009**, *129*, 12–19. [CrossRef]

15. Martins, P.M.; Gomez, V.; Lopes, A.C.; Tavares, C.J.; Botelho, G.; Irusta, S.; Lanceros-Mendez, S. Improving photocatalytic performance and recyclability by development of Er-doped and Er/Pr-codoped TiO_2/Poly(vinylidene difluoride)–trifluoroethylene composite membranes. *J. Phys. Chem. C* **2014**, *118*, 27944–27953. [CrossRef]

16. Barakat, M.A.; Kumar, R. Photocatalytic activity enhancement of titanium dioxide nanoparticles. In *Photocatalytic Activity Enhancement of Titanium Dioxide Nanoparticles*; Springer: Berlin, Germany, 2016; pp. 1–29.

17. Almeida, N.A.; Martins, P.M.; Teixeira, S.; Lopes da Silva, J.A.; Sencadas, V.; Kühn, K.; Cuniberti, G.; Lanceros-Mendez, S.; Marques, P.A.A.P. TiO_2/graphene oxide immobilized in P(VDF-TrFE) electrospun membranes with enhanced visible-light-induced photocatalytic performance. *J. Mater. Sci.* **2016**, *51*, 6974–6986. [CrossRef]

18. Li, X.; Wang, C.; Xia, N.; Jiang, M.; Liu, R.; Huang, J.; Li, Q.; Luo, Z.; Liu, L.; Xu, W.; et al. Novel ZnO-TiO2 nanocomposite arrays on Ti fabric for enhanced photocatalytic application. *J. Mol. Struct.* **2017**, *1148*, 347–355. [CrossRef]

19. Momeni, M.M.; Ghayeb, Y. Fabrication, characterization and photocatalytic properties of Au/TiO2-WO3 nanotubular composite synthesized by photo-assisted deposition and electrochemical anodizing methods. *J. Mol. Catal. A Chem.* **2016**, *417*, 107–115. [CrossRef]

20. Momeni, M.M. Fabrication of copper decorated tungsten oxide-titanium oxide nanotubes by photochemical deposition technique and their photocatalytic application under visible light. *Appl. Surf. Sci.* **2015**, *357*, 160–166. [CrossRef]

21. Momeni, M.M.; Ghayeb, Y. Cobalt modified tungsten–titania nanotube composite photoanodes for photoelectrochemical solar water splitting. *J. Mater. Sci. Mater. Electron.* **2016**, *27*, 3318–3327. [CrossRef]

22. Angkaew, S.; Limsuwan, P. Preparation of silver-titanium dioxide core-shell (Ag@TiO_2) nanoparticles: Effect of Ti-Ag mole ratio. *Procedia Eng.* **2012**, *32*, 649–655. [CrossRef]

23. Daskalaki, V.M.; Antoniadou, M.; Li Puma, G.; Kondarides, D.I.; Lianos, P. Solar light-responsive Pt/CdS/TiO2 photocatalysts for hydrogen production and simultaneous degradation of inorganic or organic sacrificial agents in wastewater. *Environ. Sci. Technol.* **2010**, *44*, 7200–7205. [CrossRef]

24. Bian, Z.; Tachikawa, T.; Kim, W.; Choi, W.; Majima, T. Superior electron transport and photocatalytic abilities of metal-nanoparticle-loaded TiO_2 superstructures. *J. Phys. Chem. C* **2012**, *116*, 25444–25453. [CrossRef]

25. Tian, Y.; Tatsuma, T. Mechanisms and applications of plasmon-induced charge separation at TiO_2 films loaded with gold nanoparticles. *J. Am. Chem. Soc.* **2005**, *127*, 7632–7637. [CrossRef] [PubMed]

26. Seh, Z.W.; Liu, S.; Low, M.; Zhang, S.-Y.; Liu, Z.; Mlayah, A.; Han, M.-Y. Janus Au-TiO_2 photocatalysts with strong localization of plasmonic near-fields for efficient visible-light hydrogen generation. *Adv. Mater.* **2012**, *24*, 2310–2314. [CrossRef] [PubMed]

27. Al-Akraa, I.M.; Mohammad, A.M.; El-Deab, M.S.; El-Anadouli, B.E. Flower-shaped gold nanoparticles: Preparation, characterization, and electrocatalytic application. *Arab. J. Chem.* **2017**, *10*, 877–884. [CrossRef]

28. Santhoshkumar, J.; Rajeshkumar, S.; Venkat Kumar, S. Phyto-assisted synthesis, characterization and applications of gold nanoparticles—A review. *Biochem. Biophys. Rep.* **2017**, *11*, 46–57. [CrossRef] [PubMed]

29. Haruta, M. Catalysis of gold nanoparticles deposited on metal oxides. *Cattech* **2002**, *6*, 102–115. [CrossRef]

30. Thompson, D.T. Using gold nanoparticles for catalysis. *Nano Today* **2007**, *2*, 40–43. [CrossRef]

31. Barakat, T.; Rooke, J.C.; Genty, E.; Cousin, R.; Siffert, S.; Su, B.-L. Gold catalysts in environmental remediation and water-gas shift technologies. *Energy Environ. Sci.* **2013**, *6*, 371–391. [CrossRef]

32. Okumura, M.; Tanaka, K.; Ueda, A.; Haruta, M. The reactivities of dimethylgold(III)β-diketone on the surface of TiO2: A novel preparation method for Au catalysts. *Solid State Ion.* **1997**, *95*, 143–149. [CrossRef]

33. Su, R.; Tiruvalam, R.; He, Q.; Dimitratos, N.; Kesavan, L.; Hammond, C.; Lopez-Sanchez, J.A.; Bechstein, R.; Kiely, C.J.; Hutchings, G.J.; et al. Promotion of phenol photodecomposition over TiO_2 using Au, Pd, and Au–Pd nanoparticles. *ACS Nano* **2012**, *6*, 6284–6292. [CrossRef] [PubMed]

34. Haugen, A.B.; Kumakiri, I.; Simon, C.; Einarsrud, M.-A. TiO2, TiO2/Ag and TiO2/Au photocatalysts prepared by spray pyrolysis. *J. Eur. Ceram. Soc.* **2011**, *31*, 291–298. [CrossRef]

35. Chandrasekharan, N.; Kamat, P.V. Assembling gold nanoparticles as nanostructured films using an electrophoretic approach. *Nano Lett.* **2001**, *1*, 67–70. [CrossRef]

36. Fackler, J.P. Catalysis by Gold By Geoffrey C. Bond (Brunel University, U.K.), Catherine Louis (Université Pierre et Marie Curie, France), and David, T. Thompson (Consultant, World Gold Council, UK). From the Series: Catalytic Science Series, Volume 6. Series Edited by Graham J. Hutchings. Imperial College Press: London. 2006. xvi + 366 pp. ISBN 1-86094-658-5. *J. Am. Chem. Soc.* **2007**, *129*, 4107. [CrossRef]

37. Luna, M.; Gatica, J.M.; Vidal, H.; Mosquera, M.J. One-pot synthesis of Au/N-TiO2 photocatalysts for environmental applications: Enhancement of dyes and NOx photodegradation. *Powder Technol.* **2019**, *355*, 793–807. [CrossRef]

38. Zhu, H.; Chen, X.; Zheng, Z.; Ke, X.; Jaatinen, E.; Zhao, J.; Guo, C.; Xie, T.; Wang, D. Mechanism of supported gold nanoparticles as photocatalysts under ultraviolet and visible light irradiation. *Chem. Commun.* **2009**, 7524–7526. [CrossRef]

39. Kamely, N.; Ujihara, M. Confeito-like Au/TiO$_2$ nanocomposite: Synthesis and plasmon-induced photocatalysis. *J. Nanoparticle Res.* **2018**, *20*, 172. [CrossRef]

40. Li, J.; Zeng, H.C. Preparation of monodisperse Au/TiO$_2$ nanocatalysts via self-assembly. *Chem. Mater.* **2006**, *18*, 4270–4277. [CrossRef]

41. D'Amato, C.A.; Giovannetti, R.; Zannotti, M.; Rommozzi, E.; Ferraro, S.; Seghetti, C.; Minicucci, M.; Gunnella, R.; Di Cicco, A. Enhancement of visible-light photoactivity by polypropylene coated plasmonic Au/TiO$_2$ for dye degradation in water solution. *Appl. Surf. Sci.* **2018**, *441*, 575–587. [CrossRef]

42. Singh, J.; Manna, A.K.; Soni, R.K. Bifunctional Au–TiO$_2$ thin films with enhanced photocatalytic activity and SERS based multiplexed detection of organic pollutant. *J. Mater. Sci. Mater. Electron.* **2019**, *30*, 16478–16493. [CrossRef]

43. Mompelat, S.; Le Bot, B.; Thomas, O. Occurrence and fate of pharmaceutical products and by-products, from resource to drinking water. *Environ. Int.* **2009**, *35*, 803–814. [CrossRef] [PubMed]

44. Pereira, A.M.P.T.; Silva, L.J.G.; Meisel, L.M.; Lino, C.M.; Pena, A. Environmental impact of pharmaceuticals from Portuguese wastewaters: Geographical and seasonal occurrence, removal and risk assessment. *Environ. Res.* **2015**, *136*, 108–119. [CrossRef] [PubMed]

45. Song, M.; Bian, L.; Zhou, T.; Zhao, X. Surface ζ potential and photocatalytic activity of rare earths doped TiO$_2$. *J. Rare Earths* **2008**, *26*, 693–699. [CrossRef]

46. Sentein, C.; Guizard, B.; Giraud, S.; Yé, C.; Ténégal, F. Dispersion and stability of TiO2nanoparticles synthesized by laser pyrolysis in aqueous suspensions. *J. Phys. Conf. Ser.* **2009**, *170*, 012013. [CrossRef]

47. Chen, W.; Zhang, J.; Cai, W. Sonochemical preparation of Au, Ag, Pd/SiO$_2$ mesoporous nanocomposites. *Scr. Mater.* **2003**, *48*, 1061–1066. [CrossRef]

48. Kuge, K.i.; Calzaferri, G. Gold-loaded zeolite A. *Microporous Mesoporous Mater.* **2003**, *66*, 15–20. [CrossRef]

49. Mihai, S.; Cursaru, D.; Ghita, D.; Dinescu, A. Morpho ierarhic TiO$_2$ with plasmonic gold decoration for highly active photocatalysis properties. *Mater. Lett.* **2016**, *162*, 222–225. [CrossRef]

50. Cojocaru, B.; Andrei, V.; Tudorache, M.; Lin, F.; Cadigan, C.; Richards, R.; Parvulescu, V.I. Enhanced photo-degradation of bisphenol pollutants onto gold-modified photocatalysts. *Catal. Today* **2017**, *284*, 153–159. [CrossRef]

51. Kumar, S.G.; Devi, L.G. Review on modified TiO2 photocatalysis under UV/visible light: Selected results and related mechanisms on interfacial charge carrier transfer dynamics. *J. Phys. Chem. A* **2011**, *115*, 13211–13241. [CrossRef]

52. Lu, M. *Photocatalysis and Water Purification: From Fundamentals to Recent Applications*; John Wiley & Sons: Hoboken, NJ, USA, 2013.

53. Wang, H.; Faria, J.L.; Dong, S.; Chang, Y. Mesoporous Au/TiO$_2$ composites preparation, characterization, and photocatalytic properties. *Mater. Sci. Eng. B* **2012**, *177*, 913–919. [CrossRef]

54. Wang, X.; Caruso, R.A. Enhancing photocatalytic activity of titania materials by using porous structures and the addition of gold nanoparticles. *J. Mater. Chem.* **2011**, *21*, 20–28. [CrossRef]

55. Wongwisate, P.; Chavadej, S.; Gulari, E.; Sreethawong, T.; Rangsunvigit, P. Effects of monometallic and bimetallic Au–Ag supported on sol–gel TiO2 on photocatalytic degradation of 4-chlorophenol and its intermediates. *Desalination* **2011**, *272*, 154–163. [CrossRef]

56. Scarabelli, L.; Sánchez-Iglesias, A.; Pérez-Juste, J.; Liz-Marzán, L.M. A "tips and tricks" practical guide to the synthesis of gold nanorods. *J. Phys. Chem. Lett.* **2015**, *6*, 4270–4279. [CrossRef] [PubMed]

57. Emeline, A.V.; Ryabchuk, V.; Serpone, N. Factors affecting the efficiency of a photocatalyzed process in aqueous metal-oxide dispersions: Prospect of distinguishing between two kinetic models. *J. Photochem. Photobiol. A Chem.* **2000**, *133*, 89–97. [CrossRef]

58. Evgenidou, E.; Fytianos, K.; Poulios, I. Semiconductor-sensitized photodegradation of dichlorvos in water using TiO$_2$ and ZnO as catalysts. *Appl. Catal. B Environ.* **2005**, *59*, 81–89. [CrossRef]

59. Le, H.N.; Babick, F.; Kühn, K.; Nguyen, M.T.; Stintz, M.; Cuniberti, G. Impact of ultrasonic dispersion on the photocatalytic activity of titania aggregates. *Beilstein J. Nanotechnol.* **2015**, *6*, 2423–2430. [CrossRef]

60. Behnajady, M.A.; Modirshahla, N.; Hamzavi, R. Kinetic study on photocatalytic degradation of C.I. Acid Yellow 23 by ZnO photocatalyst. *J. Hazard. Mater.* **2006**, *133*, 226–232. [CrossRef]

61. Grimme, S.; Bannwarth, C.; Shushkov, P. A robust and accurate tight-binding quantum chemical method for structures, vibrational frequencies, and noncovalent interactions of large molecular systems parametrized for all spd-block elements (Z = 1–86). *J. Chem. Theory Comput.* **2017**, *13*, 1989–2009. [CrossRef]

62. Lamiel-Garcia, O.; Ko, K.C.; Lee, J.Y.; Bromley, S.T.; Illas, F. When anatase nanoparticles become bulklike: Properties of realistic TiO_2 nanoparticles in the 1–6 nm size range from all electron relativistic density functional theory based calculations. *J. Chem. Theory Comput.* **2017**, *13*, 1785–1793. [CrossRef]

63. Zhang, X.; Sun, C.Q.; Hirao, H. Guanine binding to gold nanoparticles through nonbonding interactions. *Phys. Chem. Chem. Phys.* **2013**, *15*, 19284–19292. [CrossRef]

64. Marenich, A.V.; Jerome, S.V.; Cramer, C.J.; Truhlar, D.G. Charge model 5: An extension of hirshfeld population analysis for the accurate description of molecular interactions in gaseous and condensed phases. *J. Chem. Theory Comput.* **2012**, *8*, 527–541. [CrossRef] [PubMed]

65. Green, I.X.; Tang, W.; Neurock, M.; Yates, J.T. Insights into catalytic oxidation at the Au/TiO_2 dual perimeter sites. *Acc. Chem. Res.* **2014**, *47*, 805–815. [CrossRef] [PubMed]

66. Sakthivel, S.; Hidalgo, M.C.; Bahnemann, D.W.; Geissen, S.U.; Murugesan, V.; Vogelpohl, A. A fine route to tune the photocatalytic activity of TiO_2. *Appl. Catal. B Environ.* **2006**, *63*, 31–40. [CrossRef]